J Mater Sci (2011) 46:4206–4215
DOI 10.1007/s10853-011-5426-7

IIB 2010

# First-principles study of structure, vacancy formation, and strength of bcc Fe/$V_4C_3$ interface

**Kaoru Nakamura · Toshiharu Ohnuma · Takashi Ogata**

Received: 30 September 2010 / Accepted: 1 March 2011 / Published online: 10 March 2011

**Abstract** Voids are representative of the damage process in both creep and ductile fractures. Although the matrix/precipitate interface has been considered the preferential nucleation site for voids, the relationship between the atomic structure of this interface and the nucleation mechanism of a void has never been sufficiently investigated. In this study, the bcc Fe/$V_4C_3$ interface is selected as a model interface between a matrix and precipitate. The vacancy formation energy and intrinsic mechanical strength at this interface are investigated using a first-principles calculation because they should be related with the nucleation of creep and ductile voids, respectively. Within the considered interface, the Fe vacancy is found to be dominant. When the Baker–Nutting orientation relationship is satisfied at the interface, the calculated intrinsic mechanical strength of the interface is 23.8 GPa. However, when the geometric coherence at the interface is low as compared to that of the Baker–Nutting orientation relationship, it is found that the interfacial mechanical strength is significantly weakened. At each interface, it is found that the back-bond of the interface determined the interfacial strength because of the strongly bonded Fe–C on the interface. The nucleation mechanism of a void at the matrix/precipitate interface is discussed based on the present findings. It is suggested that local decohesion at the matrix/precipitate interface should be the origin of the nucleation of a ductile void.

K. Nakamura (✉) · T. Ohnuma · T. Ogata
Central Research Institute of Electric Power Industry,
2-6-1, Nagasaka, Yokosuka, Kanagawa 240-0196, Japan
e-mail: n-kaoru@criepi.denken.or.jp

## Introduction

The nucleation of voids (or cavities) is a representative damage mechanism in the deformation of alloys. In the case of a high temperature creep condition, nucleated voids can continue to grow by vacancy diffusion along grain boundaries. Then, neighboring voids can coalesce and form micro-cracks along grain boundaries. Thus, voids can lead to tertiary creep and eventually failure [1]. Creep voids are frequently nucleated on a grain boundary where the atomic structure deviates from a perfect lattice. This indicates that the excess energy at the grain boundary helps in the nucleation of voids. In addition, it is known that void nucleation occurs more easily in commercial alloys than in pure metals [2]. This indicates that the presence of second-phase particles (precipitates or inclusions) promotes the nucleation of voids. As a consequence, it can be said that precipitations on the grain boundaries have a crucial role in the nucleation of voids under a creep condition. Actually, voids are observed at the matrix/precipitate or non-metallic inclusion interfaces [2–4]. In addition, it is reported that the planar-shaped precipitate has higher resistance for the nucleation of voids than the triangular-shaped precipitate on the grain boundaries [5]. Therefore, it is significant to understand the detailed mechanism that promotes the nucleation of voids at these interfaces. In addition, voids nucleate during tensile deformation and lead to ductile failure. Moreover, in this case, a hetero-phase interface such as a ferrite/martensite interface [6] and precipitates [7] play major roles in the nucleation of ductile voids. In contrast to creep deformation, tensile deformation does not necessarily involve a thermally activated vacancy diffusion process. Instead, decohesion at the interface is related to the nucleation of ductile voids [8, 9].

Therefore, it is significant to investigate the mechanical strength of the interface and the interfacial decohesion mechanism. The accumulation of detailed information, especially at the atomic level, is expected to provide useful insights for the development of alloys with higher strengths by controlling the types, sizes, and morphologies of precipitates.

Recently, Ogata et al. reviewed numerous atomistic simulations that investigated the intrinsic mechanical strengths and deformation mechanisms of various interfaces [10]. However, in the case of Fe, atomistic investigations of the Fe/carbide interface have been quite limited (TiC [11–14], ZrC [15], and NbC [16]), even though carbide precipitation strengthened steel is widely used [17–19]. This situation is partly because of the difficulty of high resolution transmission electron microscope (HRTEM) observations of an interfacial atomic structure as the result of the magnetic moment. Moreover, a reliable inter-atomic potential between the Fe, alloying element, and C is lacking. This situation makes it quite difficult to use direct molecular dynamic simulation to simulate the nucleation of voids at a Fe/carbide interface. Therefore, in this study, the vacancy formation energy and intrinsic mechanical strength at a bcc Fe/$V_4C_3$ interface were investigated. Here, a first-principles calculation was employed because, across the metal/carbide interface, the character of the chemical bonding is suddenly changed from metallic bonding to covalent or ionic bonding. The vacancy formation energy at the interface is thought to be directly associated with creep voids because creep voids are considered to nucleate by the accumulation of vacancies. On the other hand, the intrinsic mechanical strength, which is the interfacial strength at 0 K excluding the effect of any defects, is associated with the nucleation of ductile voids.

Vanadium carbide is one of the popular precipitates in high strength steel. In addition, $V_4C_3$ is reported to promote the nucleation of creep voids [20]. The present authors have also observed nucleated creep voids next to $V_4C_3$ precipitates in creep-interrupted Cr–Mo–V forged steel [21]. Often, vanadium carbide is referred to as $VC_x$ because of the carbon vacancies [22] and is frequently called $V_4C_3$ in the popular high strength steels [23–25]. $V_4C_3$ precipitates have a plate-like shape in the grain interior because a favorable Baker–Nutting type orientation relationship [26] can be satisfied between the matrix bcc Fe and $V_4C_3$ [27–29]. In contrast, at a grain boundary, the precipitate shape is rather spherical because of the influence of the orientation of the neighboring crystals across the grain boundary. Therefore, it can be theorized that the interfacial property of the bcc Fe/$V_4C_3$ interface is strongly dependent on the orientation relationship. This study is a first step to understand the atomistic mechanism for the nucleation of voids at a matrix/precipitate interface.

## Calculation procedure

A plane-wave-based PAW method implemented in VASP code [30] was used to calculate structural relaxation and precisely determine the total energy. The entire system, including the Fe atom, was calculated using spin polarization. The exchange–correlation functional was described by a generalized gradient approximation (GGA) of the PBE form [31, 32]. The plane-wave cut-off energy was set to 400 eV throughout the calculation. The numerical error was estimated to be about 1 meV/atom for a bcc Fe unit cell by convergence tests of the cut-off energy. For the metallic occupation, the Methfessel–Paxton scheme [33] was used, with a smearing width of 0.2 eV. The Monkhorst–Pack scheme [34] was used for *k*-point sampling. The density of the *k*-points was determined to ensure that the convergence of energy became $<0.1$ meV/atom. A force of $<10^{-2}$ eV/Å and a total energy change of $10^{-8}$ eV were selected as the convergence criteria for the structural optimization. The calculated lattice constants (and experimental values) for bcc Fe, bcc V, and $V_4C_3$ were 2.833 (2.865 [35]), 2.979 (3.024 [36]), and 4.109 (4.149 [37]) Å, respectively. These errors are within the standard error for a first-principles calculation using GGA.

Figure 1 shows the crystal structures of (a) bcc Fe and (b) $V_4C_3$. The parallel planes and directions of each crystal in the Baker–Nutting orientation relationship are also drawn. The atomic structure and charge density plot shown later were drawn using VESTA software [38]. First, the geometrical coherence at the interface was evaluated using the coincidence reciprocal lattice point (CRLP) method [39] to confirm that the Baker–Nutting orientation relationship was the most favorable. In the CRLP method, the geometrical coherence between two crystals can be evaluated by the sum of the overlap volume between reciprocal spheres derived from them. Here, a reciprocal sphere is defined as a reciprocal point with artificial size. A geometrically favorable orientation relationship can be predicted as rotating one crystal in two orthogonal directions, while the other crystal is fixed. The size of the reciprocal sphere and the maximum mirror index of two crystals that generate a finite reciprocal lattice were examined to acquire the converged result. So far, the validity of the CRLP method has been shown for a number of metal/ceramic interfaces [40–44]. However, no atomistic relaxation effect or consideration of the termination plane at the interface is included in the CRLP method. In Fig. 1b, there are two types (001) layers in $V_4C_3$. One is a VC layer, where the numbers of V atoms and C atoms are equal. The other is a $V_2C$ layer, where number of C atoms is half that of the V atoms. Each termination layer must be considered to determine the most stable atomic structure for the bcc Fe/$V_4C_3$ interface. In addition, a rigid body translation

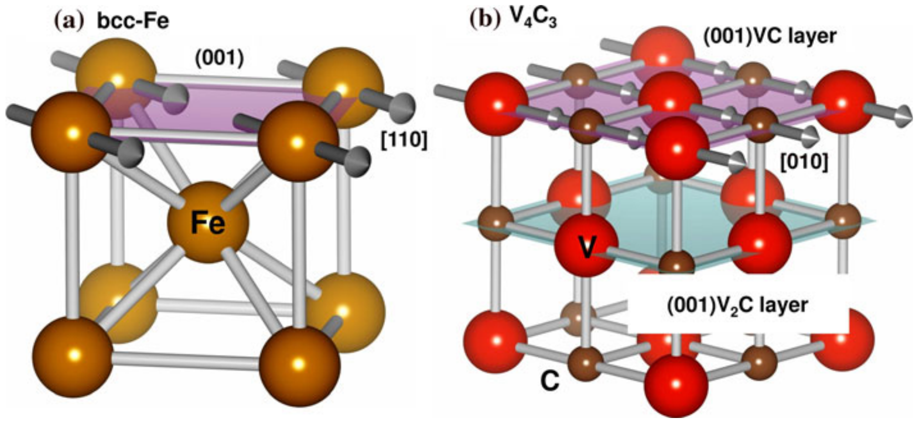

**Fig. 1** Schematic illustration of **a** bcc Fe and **b** $V_4C_3$ crystal structure. The parallel plane and direction in the Baker–Nutting type orientation relationship are also shown

parallel to the interface must be considered to determine the most stable interfacial atomic structure. In the present study, only high symmetry translation states were considered because Fe and C atoms are expected to form strongly directional bonds. Here, a unit vector of bcc Fe along the [110] direction is defined as **Tx** and that along the $[1\bar{1}0]$ direction is defined as **Ty**. The candidate translation states are as follows: (a) Fe–C on top: (**Tx**,**Ty**) = (0.5,0); (b) Fe–V on top: (**Tx**,**Ty**) = (0,0); (c) Fe–VC hollow: (**Tx**,**Ty**) = (0.25,0.25) for the VC plane; (d) Fe–C on top and Fe–VC hollow: (**Tx**,**Ty**) = (0,0); (e) Fe–V on top: (**Tx**,**Ty**) = (0.5,0); (f) Fe–VC hollow: (**Tx**,**Ty**) = (0.25,0.25) for the $V_2C$ plane. Each model of the bcc Fe/$V_4C_3$ interface was constructed using the supercell approach. The atomic structure of the interface was fully relaxed, including the atomic position and cell shape. A 5 × 5 × 1 reciprocal *k*-point mesh was selected (the irreducible *k*-points were 6 or 9) because the equivalent interfaces in the supercell needed to be substantially separated so as not to interact with each other.

As the number of atoms in the supercell was dependent on the termination plane in $V_4C_3$, it was not appropriate to evaluate the energetic stability of the interface based only on the total energy. Therefore, the work of separation, $W_{\mathrm{sep}}$, was calculated as follows and used to discuss the energetic stability of the interface

$$W_{\mathrm{sep}} = \left(E^{\mathrm{tot}}_{\mathrm{surf,Fe}} + E^{\mathrm{tot}}_{\mathrm{surf,V_4C_3}} - E^{\mathrm{tot}}_{\mathrm{inter,Fe/V_4C_3}}\right)/2A_{\mathrm{inter}}, \qquad (1)$$

where $E^{\mathrm{tot}}_{\mathrm{inter,Fe/V_4C_3}}$ is the total energy of the relaxed interfacial supercell and $E^{\mathrm{tot}}_{\mathrm{surf,Fe}}$, $E^{\mathrm{tot}}_{\mathrm{surf,V_4C_3}}$ are the total energies of the relaxed surface slabs with equivalent termination planes to the supercell, including the interface, respectively. $A_{\mathrm{inter}}$ is the area of the interface in the supercell. The division by 2 in Eq. 1 was performed because there were two equivalent interfaces in one supercell as a result of the periodic boundary condition. Systematic convergence tests were performed with increases in the number of stacking periods perpendicular to the interface in both bcc Fe and $V_4C_3$ until the work of separation was sufficiently converged.

## Results and discussion

### Energetic stability of the interface

Figure 2 shows the predicted geometric coherence map normalized by the maximum overlap volume. The initial orientation relationship was as follows: $(001)_{\mathrm{Fe}}//(001)_{\mathrm{V_4C_3}}$, $[001]_{\mathrm{Fe}}//[001]_{\mathrm{V_4C_3}}$. Obviously, it can be seen that the Baker–Nutting orientation relationship (45° rotation) was the most coherent and there was no favorable state except for the highly symmetric rotation state. This agreement between the prediction of a favorable orientation relationship by the CRLP method and the experimental observation indicates that the simple geometry for the atomic configuration was dominant in the bcc Fe/$V_4C_3$ interface. This originated in the directional covalent bonding between Fe and C across the interface. This CRLP map was further used to select the orientation relationship, which represents a bcc Fe/$V_4C_3$ disordered model interface on the grain boundary, as shown later.

Figure 3 shows the calculated $W_{\mathrm{sep}}$ from Eq. 1 as a function of the number of stacking periods in bcc Fe and $V_4C_3$. It was confirmed that the surface energies of bcc Fe and $V_4C_3$ were converged below 0.01 J/m$^2$ and each $W_{\mathrm{sep}}$ was converged below 0.1 J/m$^2$ when the number of stacking periods was four. A general trend can be drawn from Fig. 3 that the Fe–C bond perpendicular to the interface greatly contributes to the stability of the interface, while the Fe–V bond has a contrary role. Figure 4 shows the relaxed interfacial atomic structures when the number of stacking periods was four in both bcc Fe and $V_4C_3$. The number of atoms in each interface supercell was 54 for the VC termination and 49 for the $V_2C$ termination. All interfaces appear to have a simple structure because of the highly ordered Baker–Nutting orientation relationship.

**Fig. 2** Three-dimensional geometric coherence map between bcc Fe and $V_4C_3$ crystals. The *horizontal axes* represent the rotation angles around the [001] and [100] directions of bcc Fe, and the *vertical axis* is the overlap volume normalized by the maximum value

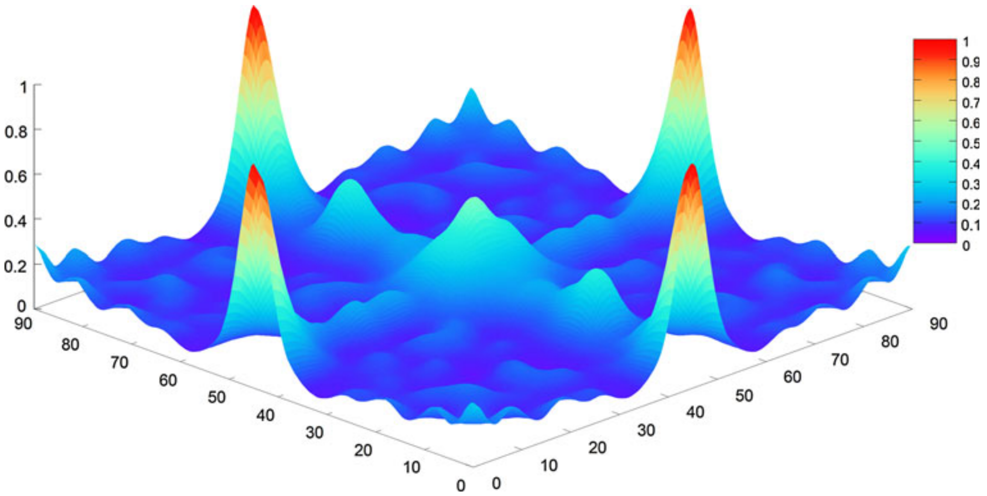

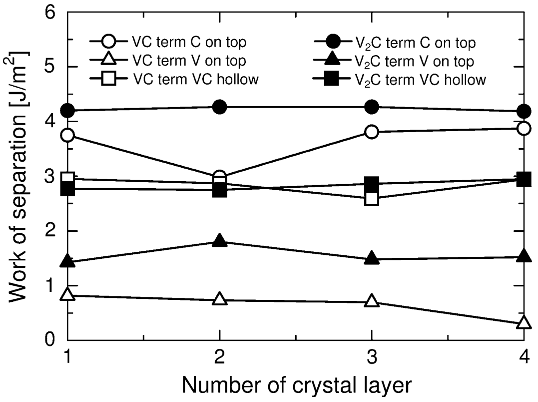

**Fig. 3** Calculated $W_{sep}$ of considered interfaces as function of number of stacking periods to interface in bcc Fe and $V_4C_3$

However, the $W_{sep}$ values of these structures are quite different. Across the interface, the length of the Fe–C bond is 1.805 Å at the most stable $V_2C$ terminated C on top interface shown in Fig. 4d. The length of the Fe–V bond is 2.623 Å at the most unstable VC terminated V on top interface shown in Fig. 4b, which indicates that repulsive interaction between the Fe atom and V atom induces a relatively large interfacial separation. The VC terminated C on top interface also shows a high $W_{sep}$, but is slightly unstable compared with the $V_2C$ terminated C on top interface. As the $V_2C$ terminated C on top interface has a hollow site in the middle of the termination plane in the $V_4C_3$ side, the Fe atom centered in the middle of the interface can move inward to the $V_4C_3$ side so as not to bend the V–C bond. In the case of the VC terminated C on top interface, if the Fe atom at the interface moves toward the $V_4C_3$ side in order to make the bond with the C atom stronger, it will induce a strain because of the bending of the V–C bond. Actually, the length of the Fe–C bond across the interface is 1.872 Å at the VC terminated C on top interface shown in Fig. 4a, which is 4% longer than that at the $V_2C$ terminated C on top interface shown in Fig. 4d. This difference in the bond lengths is thought to be mainly related to the stability difference between the $V_2C$ terminated C on top interface and the VC terminated C on top interface. Because of the d–p bonding between the Fe atom and C atom, the preferential bonding direction of the Fe–C across the interface is perpendicular to the interface, rather than the inclined direction found in the V on top and VC hollow interface. The former bonding corresponds to the bond between the interstitial C atom and the surrounding atoms in the bcc crystal. The latter bonding corresponds to the bond formed in a perfect bcc crystal. It is well known that the C atom is the representative interstitial element in steel. In contrast, because of the d–d interaction between the Fe atom and V atom, the Fe–V bond does not prefer the perpendicular direction to the interface but prefers bcc-like bonding. Therefore, it can be easily understood that the V on top interface is unstable. In particular, in the most unstable VC terminated V on top interface shown in Fig. 4b, the density of the unstable F–C bond is higher than that of the $V_2C$ terminated V on top interface shown in Fig. 4e. As the density of the Fe–V bond is the same for these two interfaces, it can be said that the unstable Fe–C bond largely contributes to the difference in energetic stability between the VC terminated V on top interface and $V_2C$ terminated V on top interface, as shown in Fig. 3. The order of the energetic stability of the hollow interfaces is positioned between the C on top and the V on top interfaces because a stable F–V bond and unstable Fe–C bond are formed.

## Vacancy formation energy

Under diffusion creep, nucleated voids are known to take a penny-shape form [1]. If only the decohesion of the

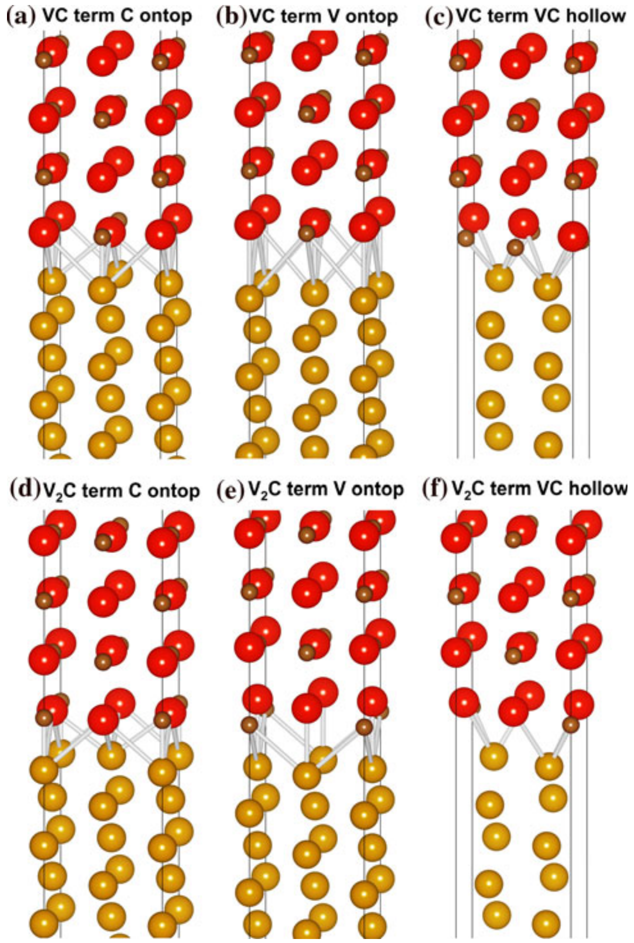

**Fig. 4** Relaxed atomic structures of considered bcc Fe/$V_4C_3$ interface. The lower side is the Fe crystal and the upper side is the $V_4C_3$ crystal. The Fe–C bond and F–V bond across the interface are drawn as *sticks*

matrix/precipitate interface was involved in the nucleation of creep voids, the shape would be crack-like. Raj and Ashby modeled the nucleation of voids using the vacancy accumulation mechanism [45]. Moreover, vacancies play a significant role during creep deformation because they help with the diffusion of the alloying element and induce Ostwald ripening, which decreases the resistance to dislocation motion. This time-dependent change in precipitations is frequently mentioned in relation to the degradation of materials. In particular, the grain boundary or hetero-phase interface is thought to be a source and sink of vacancies. Therefore, the vacancy formation energies at the bcc Fe/$V_4C_3$ interface and Fe grain boundary were calculated.

Here, two types of bcc Fe/$V_4C_3$ interfaces were selected. One was the most stable $V_2C$ terminated C on top interface shown in Fig. 4d. This interface is a representative ordered matrix/precipitate interface within the grain interior and can be referred to as an ordered interface. The other was the assumed representative disordered matrix/precipitate interface on the grain boundary. The geometric coherence map shown in Fig. 2 was used to determine such an orientation relationship with low coherence. The determined orientation relationship between the bcc Fe and $V_4C_3$ was as follows: $(001)_{\mathrm{Fe}}//(120)_{\mathrm{V_4C_3}}$, $[110]_{\mathrm{Fe}}//[001]_{\mathrm{V_4C_3}}$, $[1\bar{1}0]_{\mathrm{Fe}}//[2\bar{1}0]_{\mathrm{V_4C_3}}$. In this orientation relationship, the sum of the overlap volume calculated using the CRLP method was only 21% of that in the case of the Baker–Nutting orientation relationship. In addition, it should be noticed that the above orientation relationship may be fulfilled when $V_4C_3$ precipitates on the Σ 5 [001] (210) grain boundary in bcc Fe. When a disordered interface supercell was constructed, the bcc Fe lattice was repeated for two periods along the $[1\bar{1}0]$ direction in order to reduce the misfit strain as much as possible, but 13.3% remained. As a simplification, $V_4C_3$ and bcc Fe lattices were stacked for two and three periods along each respective [001] direction, which made it possible to treat a complex disordered interface with only 67 atoms. A 5 × 3 × 1 *k*-point mesh was used for integration in the Brillouin zone and the irreducible *k*-point was 6, which is the same as the ordered interface. The atomic structure of the relaxed disordered interface is shown in Fig. 5b. Because of the previously discussed favorable direction of the bond, the stacking of the Fe atoms along the [001] direction was inclined during the structure relaxation. The calculated $W_{\mathrm{sep}}$ value of the disordered interface was 3.21 J/m$^2$, which was higher than the V on top interfaces and comparable to the hollow interfaces shown in Fig. 3. Even though the atomic structure was disordered, Fe–V and Fe–C bonds with a favorable direction across the interface contributed to the relatively high energetic stability of the disordered bcc Fe/$V_4C_3$ interface.

When the vacancy formation energy at the interface was evaluated, the supercells were expanded further to reduce the artificial interaction between the vacancies in neighboring supercells. In the present calculation, the ordered interface was repeated for two periods along the two orthogonal directions parallel with the interface, and the disordered interface was repeated along the [001] direction of $V_4C_3$. The expanded supercells were composed of 196 atoms in the ordered interface and 134 atoms in the disordered interface. The distance between the introduced vacancies over the supercells was more than 8 Å. Because of a simplification, only the Γ point was used for the *k*-point sampling. In addition, the bcc Fe Σ 5 [001] (210) grain boundary was also considered to be a pure grain boundary area next to the precipitated $V_4C_3$. In the supercell of the Σ 5 grain boundary, the unit cell of bcc Fe was repeated for three periods along the $[02\bar{1}]$ direction, perpendicular to the grain boundary plane. The number of

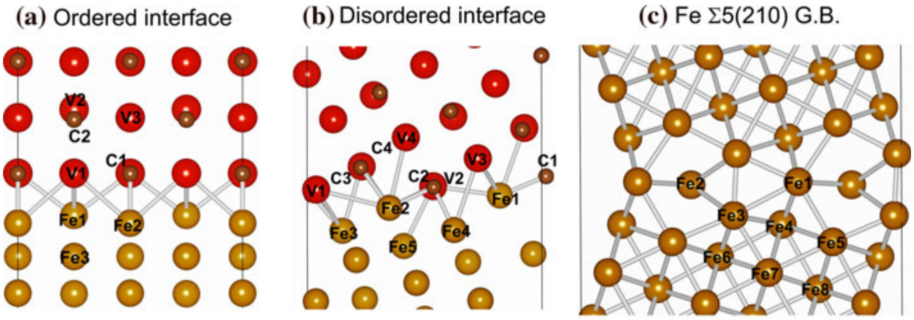

**Fig. 5** Considered sites for vacancies at bcc Fe/$V_4C_3$ **a** ordered interface, **b** disordered interface, and **c** Fe Σ 5 (210) grain boundary. The calculated vacancy formation energies at each structure are also tabulated

| | |
|---|---|
| Fe1 | -0.08 |
| Fe2 | -0.25 |
| Fe3 | 0.83 |
| V1 | 1.07 |
| V2 | 2.24 |
| V3 | 0.99 |
| C1 | -0.30 |
| C2 | -2.47 |

| | |
|---|---|
| Fe1 | 0.11 |
| Fe2 | 2.59 |
| Fe3 | -0.23 |
| Fe4 | 1.26 |
| Fe5 | 0.61 |
| V1 | 2.89 |
| V2 | 4.49 |
| V3 | 2.85 |

| | |
|---|---|
| V4 | 5.44 |
| C1 | 0.49 |
| C2 | 0.99 |
| C3 | -0.56 |
| C4 | 0.25 |

| | |
|---|---|
| Fe1 | 0.66 |
| Fe2 | 1.67 |
| Fe3 | -0.16 |
| Fe4 | 1.56 |
| Fe5 | 1.80 |
| Fe6 | 2.42 |
| Fe7 | 0.81 |
| Fe8 | 2.13 |

atoms in the supercell was 60. Before calculating the vacancy formation energy at the Σ 5 grain boundary, rigid body translation states in the grain boundary plane were systematically investigated to determine the most stable atomic structure for the grain boundary. In order to reduce the interaction between vacancies, the obtained relaxed structure of the Σ 5 grain boundary was further repeated for two periods along the $[0\bar{1}2]$ direction parallel to the grain boundary plane. A 5 × 1 × 1 *k*-point mesh was used because only one period was taken along the [100] direction.

Figure 5a–c shows the considered vacancy sites at the ordered and disordered bcc Fe/$V_4C_3$ interface and the Σ 5 grain boundary. The calculated vacancy formation energy is also shown below each structure in Fig. 5. Here, the vacancy formation energy was calculated using the following equation

$$E_{f,\mathrm{X}} = \left(E_{\mathrm{X}}^{\mathrm{tot}}(n-1) + \mu_{\mathrm{X}}\right) - E_{\mathrm{X}}^{\mathrm{tot}}(n), \qquad (2)$$

where $E_{\mathrm{X}}^{\mathrm{tot}}(n-1)$ and $E_{\mathrm{X}}^{\mathrm{tot}}(n)$ are the total energies of the supercell with and without vacancies. $\mu_{\mathrm{X}}$ is the chemical potential of atom X removed from the interface. In this study, the per-atom energies of bcc Fe, bcc V, and diamond C were used for $\mu_{\mathrm{X}}$. Because of the symmetry, only two sites on the grain boundary plane and six sites belonging to one side of the grain were considered in the Fe Σ 5 grain boundary, as shown in Fig. 5c. The calculated vacancy formation energy at the bcc Fe/$V_4C_3$ interface was very site specific. Introduced vacancies created states in the anti-bonding and nonbonding regions of the p–d hybridization band [46, 47]. When a vacancy was introduced, whether excess electrons filled the anti-bonding or non-bonding region was dependent on the environment of the surrounding chemical bonding. Thus, the physical origin of the site dependence of the vacancy formation energy is quite complex, especially for a disordered interface. Accordingly, the overall trends for vacancy formation near the interface and grain boundary are summarized in Fig. 6.

In Fig. 6, the distribution of the vacancy formation energies at the bcc Fe/$V_4C_3$ interface and Fe Σ 5 grain boundary are plotted without explicitly considering the site dependence. The dotted lines indicate Fe, V, and C vacancies in perfect bcc Fe and $V_4C_3$. Here, a 5 × 5 × 5 expanded supercell with a 3 × 3 × 3 *k*-point mesh was used for the Fe vacancies in bcc Fe. A 3 × 3 × 3 expanded supercell with a 2 × 2 × 2 *k*-point mesh was used for the V and C vacancies in $V_4C_3$. In addition, two cryptographically inequivalent V sites were considered for the V vacancies and are referred to as 1 and 2 in Fig. 6. It should

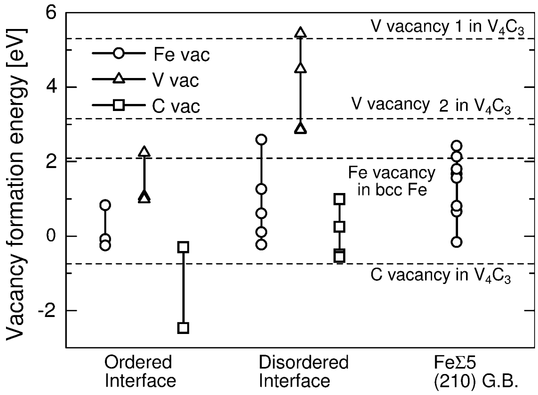

**Fig. 6** Distribution of vacancy formation energies at bcc Fe/$V_4C_3$ ordered interface, disordered interface, and Fe Σ 5 (210) grain boundary. The *dotted lines* are the vacancy formation energies in perfect bcc Fe and $V_4C_3$ crystal

be noted that the distribution of the vacancy formation energy at the disordered interface was positioned on the higher energy side than that at the ordered interface, especially for the C and V vacancies. This indicates that the V and C atoms at the disordered interface were strongly bound by the surrounding atoms. In such a case, the charge redistribution induced by the vacancies imposed an energy penalty because of the increasing anti-bonding character of the surrounding chemical bonds. Thus, it can be said that the vacancy formation energy is not necessarily high even if an interface has a geometrically ordered structure. However, within the considered interfaces and grain boundary, it was found that the vacancy formation energy of Fe was relatively low compared with the bulk for every structure. In particular, around the $V_4C_3$ precipitates on the grain boundary, the bcc Fe/$V_4C_3$ disordered interface and Fe Σ 5 grain boundary showed similar ranges for the vacancy formation energy of Fe. Therefore, vacancies could easily accumulate near the grain boundary, not only because a bcc Fe/$V_4C_3$ disordered interface formed on the grain boundary, but also because the pure Fe grain boundary free from precipitation acted as a source of vacancies. Then, the vacancy concentration near the grain boundary would be increased by the presence of precipitates and the nucleation of creep voids would become easier. Moreover, in the case of the ordered interface, the vacancy formation energies of the Fe, V, and C were lower than that in the bulk. However, an ordered interface could be formed within the grain interior. Therefore, if the vacancy diffusion kinetics is neglected, the accumulation of vacancies at the ordered interface might be slow because their major source is just the matrix/precipitate interface under creep.

## Intrinsic mechanical strength

First-principles mechanical tests are now widely used to evaluate intrinsic mechanical strength excluding the effect of defects [10]. By comparison with the intrinsic mechanical strengths of the ordered and disordered interfaces, it was expected to qualitatively show the relationship between the interfacial atomic structure and intrinsic mechanical strength of the interface. Figure 7 shows the results of first-principles tensile tests for the ordered and disordered bcc Fe/$V_4C_3$ interfaces. As mentioned above, the work of separation of the disordered interface was comparable to that of the ordered hollow interface. However, it was found that the disordered interface had about half the strength of the ordered interface. The maximum stress of the ordered interface was 23.8 GPa at 16% strain. This value was substantially higher than that of a Ni/$ZrO_2$ (111) interface, where the maximum stress was 14.5 GPa [48], even though it was a representative interface between a Ni-base superalloy and the thermal barrier coating formed onto a gas-turbine blade. In the case of the ordered interface, the tensile stress suddenly dropped with a strain of 23–24%. This sudden relaxation of the tensile stress indicated bond breaking. In Fig. 8a–d, the charge density of the ordered interface cut at the (110) plane in the supercell is plotted. Contours are drawn with successive lines using a factor of 10 within a range of 0.003–0.3 e/Å$^3$. Atoms near the interface are numbered as shown in Fig. 8. Until the tensile stress reached a maximum value at a 16% strain, the effect of the tensile strain was localized within Fe2 and the V1 layer. At 16% strain, the length of the Fe2–V1 bond was 3.42 Å, which is sufficient for bond breaking, and is shown as a dotted line. On the other hand, the Fe1–C bond shows no remarkable elongation in Fig. 8a and b. However, at 23% strain, it was found that the effect of the tensile strain extended into the bcc Fe crystal side. During the 16% strain and 23% strain, the Fe1 atom largely moved along the perpendicular direction to the interface because of the breaking of the Fe1–Fe3 bond (3.46 Å at 23% strain). At this point, only the Fe1–C bond remained at the interface. Therefore, the charge density above the Fe2 atom was greatly decreased and appeared to be an open space. In addition, the same decrease in charge density was observed below the Fe1 atom at 23% strain in Fig. 8c. The Fe1–Fe3 bond was a back-bond to the Fe1–C bond and was already broken at 23% strain, as mentioned above. Finally, interfacial decohesion occurred from the 23% strain to the 24% strain. This decohesion was localized within the Fe1 layer and Fe2 layer because the distance between the Fe1 atom and Fe2 atom was notably changed from 3.15 Å at 23% strain to 7.74 Å at 24% strain. It is noted here that the maximum allowable elongation of the Fe–Fe bond is about 30%. Although no relaxation of tensile stress was observed, even at the 23% strain, the Fe1–Fe2 bond elongated to 3.15 Å, which was an elongation of about 28.5% compared with the stable Fe–Fe bond length in bcc Fe crystal. On the

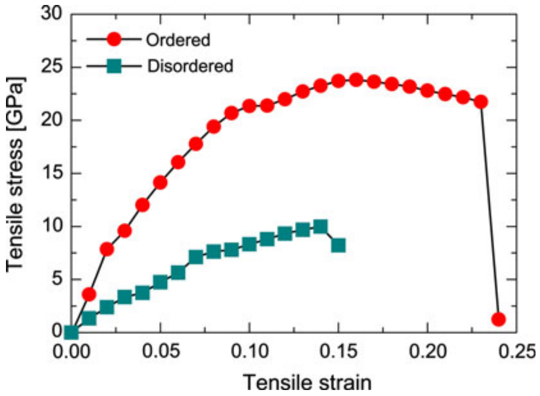

**Fig. 7** Stress–strain curve calculated using first-principles tensile test for ordered and disordered bcc Fe/$V_4C_3$ interfaces

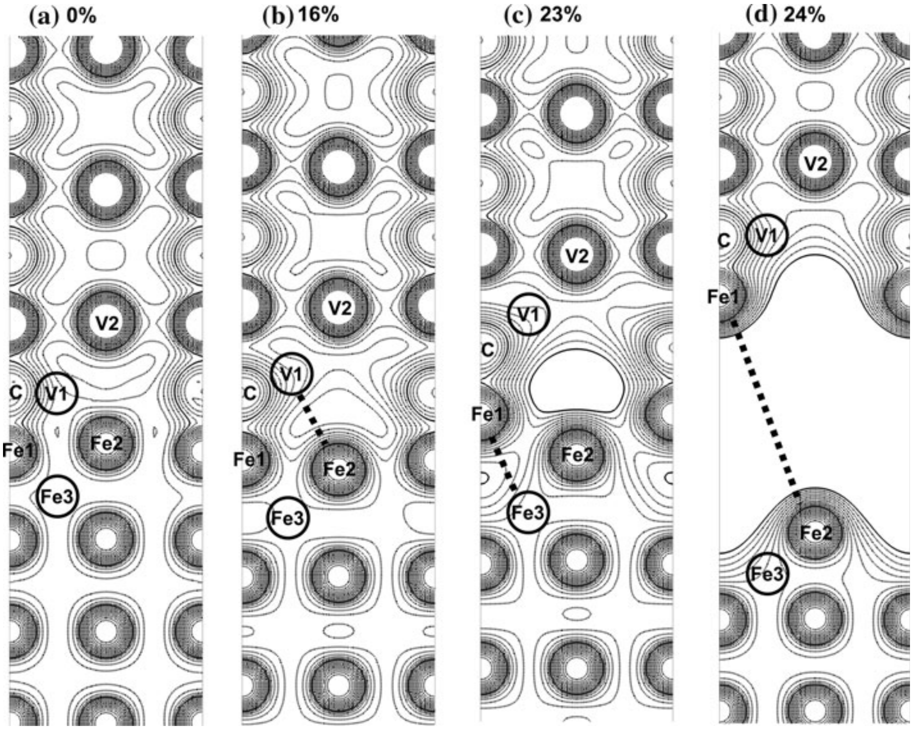

**Fig. 8** Contour map of charge density cut at (110) plane in ordered interface during first-principles tensile test. The contours are drawn with successive lines using a factor of 10 within a range of 0.003–0.3 e/Å$^3$. Selected atoms near the interface are shown by *numbers*. The *dotted lines* indicate the broken bonds

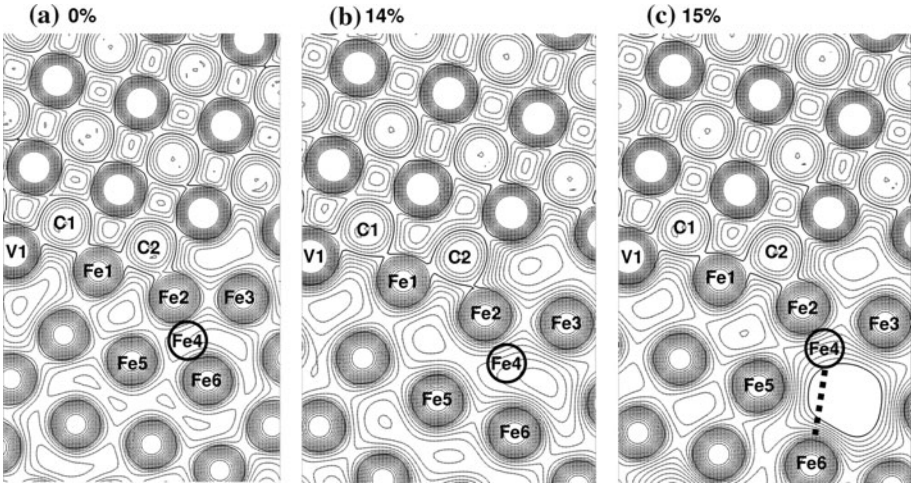

**Fig. 9** Contour map of charge density cut at (100) plane in disordered interface during first-principles tensile test. The drawing conditions are the same as Fig. 8

other hand, the Fe1–C bond remained, as shown in Fig 8d, even after the interfacial decohesion occurred. Therefore, it can be said that the Fe1–C bond did not greatly contribute to the intrinsic tensile strength of the ordered bcc Fe/$V_4C_3$ interface. Because of the strongly formed covalent bonding between the Fe1 atom and C atom, the surrounding Fe–Fe back-bond to the Fe1–C bond was thought to be weakened during the charge redistribution induced by the tensile strain.

In the case of the disordered interface, the maximum tensile stress was 10.0 GPa at 14% strain. The stress relaxation from 14% strain to 15% strain was quite small as compared with that of the ordered interface. The changes in charge density cut at the (100) plane are plotted as Fig. 9a–c with the numbered atoms near the interface. In contrast to the ordered interface, the bcc Fe crystal was homogeneously strained until the strain reached 14%. There was no bond breaking preceding the relaxation of the tensile stress. From the 14% strain to 15% strain, only the Fe4 atom and Fe6 atom were remarkably separated from each other. The length of the Fe4–Fe6 bond changed from 2.97 Å at 14% strain to 4.30 Å at 15% strain. The Fe4–Fe6 bond was the back-bond positioned at the second nearest neighbor to the Fe2–C bond formed at the interface. Therefore, the Fe4–Fe6 bond acted as the weakest link in the disordered interface. After the relaxation of the tensile stress, a large open space with a diameter of about 4 Å was introduced between the Fe4 atom and Fe6 atom at 15% strain. Because of the limitation on the size of the supercell, this introduced open space was positioned nearly at the middle on the bcc Fe crystal side. Accordingly, further tensile strain was not considered because the half area parallel with the interface was already fractured at the 15% strain. This indicates that the tensile stress should be decreased when further strain were to be applied.

If the introduced open space at the 15% strain in Fig. 9c was considered to be a ductile void, the present results of the first-principles tensile test would indicate that localized decohesion can directly induce the nucleation of voids under the ductile failure mode. Ductile voids are known to lead to fractures within the grain interior. Even if an ordered precipitate/matrix interface was formed within the grain interior, a disordered interface should also be locally formed. The tensile stress needed to introduce a ductile void was 10.0 GPa for the disordered Fe/$V_4C_3$ interface. This value was much smaller than that for an ordered interface, but seemed to be significantly larger than the external stress applied in the usual tensile test. However, hard second-phase particles, like carbide, suffer from stress concentration via the pile-up of dislocations, which makes bond breaking easier. Therefore, it can be said that geometric coherence at a matrix/precipitate interface should affect the intrinsic strength of the interface. Energetically, a lattice misfit at the interface also affects its binding strength and structural stability [49]. However, the intrinsic mechanical strength should be governed, not by the energy of the system, but by the strength of the local chemical bonds. Moreover, the chemical bonding states at the interface can be directly changed by the orientation relationship across the interface. Thus, the nucleation behavior of ductile voids should also be dependent on the geometric coherence at the matrix/precipitate interface.

However, the abovementioned mechanism cannot necessarily be applied to the nucleation of voids under high temperature creep conditions because creep voids usually nucleate under a relatively low stress condition. In order to understand the nucleation mechanism of creep voids at the atomic level, time-dependent vacancy diffusion and the interaction of vacancies must be explicitly considered under mechanical load and high temperature. In this regard, the recently developed accelerated dynamics simulation method [50] seems to be promising. We are currently developing the empirical inter-atomic potential, which can deal with the carbides in Fe by making use of the present findings. This developed potential and the direct simulation of the nucleation of voids will be reported in the near future.

## Conclusions

In this study, a bcc Fe/$V_4C_3$ interface was used to model the matrix/precipitate interface, which is considered to be the preferential nucleation site of voids. The atomic structure, vacancy formation energy, and intrinsic mechanical strength at the interface were investigated using a first-principles calculation because the vacancies and interfacial strength should be related with the nucleation of creep and ductile voids, respectively.

Using the CRLP method, it was confirmed that the Baker–Nutting orientation relationship was geometrically the most coherent in the bcc Fe/$V_4C_3$ interface. In addition, it was found that the Fe–C bond perpendicular to the interface was responsible for the energetic stability of the interface. In regard to the vacancy formation energy, it is suggested that the vacancy formation energy and geometrical coherence at the bcc Fe/$V_4C_3$ interface do not necessarily have a clear correlation. On the other hand, the interfacial mechanical strength is suggested to be dependent on the geometrical coherence at the interface. It was also found that the back-bond to the interface determines the interfacial strength because the strongly bonded Fe–C on the interface weakens the surrounding bond.

As a result, it is suggested that local decohesion at a matrix/precipitate interface should be the origin of ductile void nucleation. However, further investigation is required to understand how the accumulation of vacancies is involved in the nucleation of creep voids, particularly in relation to the temperature effect and time-dependent vacancy diffusion.

## References

1. Kassner ME, Hayes TA (2003) Int J Plast 19:1715
2. Dobrzanski J (2004) J Mater Process Technol 157–158:297
3. Wahab AA, Kral MV (2005) Mater Sci Eng A 412:222
4. Wahab AA, Hutchinson CR, Kral MV (2006) Scr Mater 55:69
5. Kim KJ, Hong HU, Min KS, Nam SW (2004) Mater Sci Eng A 387–389:531
6. Sarwar M, Priestner R (1996) J Mater Sci 31:2091. doi:10.1007/BF00356631
7. Das SK, Chatterjee S, Tarafder S (2009) J Mater Sci 44:1094. doi:10.1007/s10853-008-3106-z
8. Erdogan M (2002) J Mater Sci 37:3623. doi:10.1023/A:1016548922555
9. Oh YJ, Lee BS, Kwon SC, Hong JH (1999) J Mater Sci 34:4751. doi:10.1023/A:1004630904296
10. Ogata S, Umeno Y, Kohyama M (2010) Model Simul Mater Sci Eng 17:013001
11. Mizuno M, Tanaka I, Adachi H (1993) Acta Mater 46:1637
12. Shishidou T, Lee JH, Zhao YJ, Freeman AJ (2003) J Appl Phys 93:6876
13. Arya A, Carter EA (2003) J Chem Phys 118:8982

14. Lee JH, Shishidou T, Zhao YJ, Freeman AJ, Olson GB (2005) Philos Mag 85:3683
15. Arya A, Carter EA (2004) Surf Sci 560:103
16. Tingaud D, Maugis P (2010) Comput Mater Sci 49:60
17. Cao J, Yong Q, Liu Q, Sun X (2007) J Mater Sci 42:10080. doi: 10.1007/s10853-007-2000-4
18. Cabibo M, Fabrizi A, Merlin M, Garagnani GL (2008) J Mater Sci 43:6857. doi:10.1007/s10853-008-3000-8
19. Babu NK, Suresh MR, Sinha PP, Sarma DS (2006) J Mater Sci 41:2971. doi:10.1007/s10853-006-6718-1
20. Boniszewski T, Eaton NF (1969) Met Sci 3:103
21. Nakamura K, Ogata T (2011) J Soc Mater Sci 60:102
22. Emmons GH, Williams WS (1983) J Mater Sci 18:2589. doi: 10.1007/BF00547575
23. Locci IE, Michal GM (1988) Metall Mater Trans A 20:237
24. Maropoulous S, Karagiannis S, Ridley N (2007) J Mater Sci 42:1309. doi:10.1007/s10853-006-1191-4
25. Tsuchida Y, Inoue T, Suzuki T (2004) Int J Press Vessel Pip 81:191
26. Baker RG, Nutting J (1959) Iron Steel Inst 64:1
27. Nishida T, Tanino M (1965) J Jpn Inst Met 29:728
28. Senior BA (1988) Mater Sci Eng A 103:263
29. Yamasaki S, Bhadeshia HKDH (2003) Mater Sci Technol 19:1335
30. Kresse G, Furthmüller J (1996) Phys Rev B 54:11169
31. Perdew JP, Burke K, Ernzerhof M (1996) Phys Rev Lett 77:3865
32. Perdew JP, Burke K, Ernzerhof M (1997) Phys Rev Lett 78:1396
33. Methfessel M, Paxton AT (1989) Phys Rev B 40:3616
34. Monkhorst HJ, Pack JD (1976) Phys Rev B 13:5188
35. Zhang J, Guyot F (1999) Phys Chem Min 26:206
36. James WJ, Straumanis ME (1960) J Electrochem Soc 107:69
37. Liu H, Zhu J, Liu Y, Lai Z (2008) Mater Lett 62:3084
38. Momma K, Izumi F (2008) J Appl Crystallogr 41:653
39. Ikuhara Y, Pirouz P (1996) Mater Sci Forum 207–209:121
40. Ikuhara Y, Sugawara Y, Tanaka I, Pirouz P (1997) Interface Sci 5:5
41. Ikuhara Y, Pirouz P (1993) Ultramicroscopy 52:421
42. Ikuhara Y, Pirouz P, Heuer AH, Yadavalli S, Flynn CP (1994) Philos Mag A 70:75
43. Sasaki T, Matsunaga K, Ohta H, Hosono H, Yamamoto T, Ikuhara Y (2003) Sci Technol Adv Mater 4:575
44. Sasaki T, Matsunaga K, Ohta H, Hosono H, Yamamoto T, Ikuhara Y (2004) Mater Trans 45:2137
45. Raj R, Ashby MF (1975) Acta Metall 23:653
46. Häglund J, Guillermet AF, Grimvall G, Körling M (1993) Phys Rev B 48:11685
47. Hartford J (2000) Phys Rev B 61:2221
48. Matsunaga K, Sasaki T, Shibata N, Mizoguchi T, Yamamoto T, Ikuhara Y (2006) Phys Rev B 74:125423
49. Peng P, Jin ZH, Yang R, Hu ZQ (2004) J Mater Sci 39:3957. doi: 10.1023/B:JMSC.0000031477.24789.93
50. Voter AF, Montalenti F, Germann TC (2002) Ann Rev Mater Res 32:321